Simultaneously measured photoluminescence lifetime and quantum yield of two-photon cascade emission on single CdSe/ZnS nanocrystals

Nao Hiroshige, Toshiyuki Ihara, and Yoshihiko Kanemitsu

Phys. Rev. B **95**, 245307 — Published 12 June 2017

DOI: 10.1103/PhysRevB.95.245307

Investigation of simultaneously measured photoluminescence lifetime and quantum yield of two-photon cascade emission on single CdSe/ZnS nanocrystals

*Nao Hiroshige, Toshiyuki Ihara,[+,a)] and Yoshihiko Kanemitsu**

Institute for Chemical Research, Kyoto University, Uji, Kyoto 611-0011, Japan

The photoluminescence (PL) lifetime and quantum yield (QY) of the two-photon cascade emission (TPCE) provide critical information for assessing the quality of optoelectronic devices. The QY of TPCE has been conventionally evaluated by second-order photon correlation, $g^{(2)}$, measurements under weak-excitation conditions in single nanocrystals (NCs). Here, we report that, by measuring simultaneously both the $g^{(2)}$ and PL-decay curves, the QY of the TPCE can be determined even under strong-excitation conditions. With this technique, the effect of ionization on the QY of the TPCEs in single CdSe/ZnS NCs, which appears under strong-excitation condition, can be revealed. The obtained QYs were compared with the PL lifetime of the first and second photon emissions. We demonstrate that, even for ionized NCs, the radiative recombination rates during TPCE are almost proportional to the product of the numbers of electrons and holes.

[+] t-ihara@nict.go.jp

* kanemitu@scl.kyoto-u.ac.jp.

[a)] Present address: Advanced ICT Research Institute, National Institute of Information and Communications Technology, Kobe, 651-2492, Japan

I. INTRODUCTION

Semiconductor nanocrystals (NCs) are widely used as luminescent nanomaterials because they provide attractive optical properties for various applications [1–3]. The optical properties of NCs, such as quantum yield (QY) of photoluminescence (PL) [4–6], absorption cross section [6–10], and time-dependent PL fluctuation [11,12] have been investigated using spectroscopy on single NCs. A sequential two-photon emission, known as a two-photon cascade emission (TPCE), is a characteristic phenomenon of single NCs that occurs after the absorption of two photons [13–23]. In recent years, NCs exhibiting high luminescence quality have been synthesized [25,26]. The luminescence of the NCs is strongly influenced in optoelectronic applications by the ionization effect. Thus, studying TPCE under ionized conditions is also important [22]. When a NC is neutral, its TPCE consists of the radiative recombination of a biexciton (two electron–hole pairs) and an exciton (one electron–hole pair), as illustrated in Fig. 1(a). When an NC is ionized, the TPCE process occurs through the radiative recombination of a charged biexciton (biexciton with an additional charge) and a charged exciton (exciton with an additional charge), as shown in Fig. 1(b). TPCE has been studied not only on widely-used CdSe/ZnS and CdSe/CdS core-shell NCs [13–24] but also in various other systems, such as NCs coupled with metallic objects [27–32] and NCs with emerging materials [33–35]. Investigations of TPCE reveal much more details about the photo-absorption and recombination processes in single NCs [24], when compared to investigations of excitons. Efficient TPCE will lead to higher quality light-emitting devices, and thus, precise evaluation of the QY of TPCE is highly desirable.

One of the standard approaches for studying TPCE in single NCs is the measurement of second-order photon correlation, $g^{(2)}$, under the weak-excitation condition [13–21]. This approach works because, if the average number of the excited electron–hole pairs, $\langle N \rangle$, is much smaller than unity, the QY of the TPCE (the QY ratio between first and second photon emission during TPCE) can be directly determined from the $g^{(2)}$ curve [13,14]. If a similar technique would be available under strong-excitation condition, the use of this technique enables us to investigate various NCs whose PL QY is much lower than unity, even when using an optical setup with a low detection efficiency [16,22]. In addition, such a technique should be helpful for investigating TPCE in ionized NCs, because the ionization probability of NCs increases under strong-excitation condition [36–40]. However, the appearance of nonlinear phenomena, such as PL saturation and increased two-photon emission probabilities, makes quantitative evaluation of the TPCE QY difficult. One must establish a technique that takes into account these nonlinear effects to evaluate accurately the QY of the TPCE in the strong-excitation regime.

In this paper, we report a technique based on the simultaneous measurement of the $g^{(2)}$ and the PL-decay curves, which enables us to investigate PL lifetime and QY of the TPCE quantitatively. By accounting for the nonlinear effect of PL saturation and the increase of two-photon emission probability, the QY of TPCE in single NCs can be determined even in the strong-excitation condition. With the equations and a sophisticated analysis based on single-photon counting, we evaluated the QY of the TPCE in single CdSe/ZnS NCs for neutral and ionized conditions, which appeared under weak and strong-excitation conditions, respectively. We studied the PL lifetime of the first and second photon emission to compare their radiative recombination rates. Our results demonstrate that the radiative recombination rates during TPCE are almost proportional to the product of the numbers of electrons and holes, even when the NCs are ionized. We also discussed the difference of QY of TPCE between neutral and ionized condition.

II. EXPERIMENT

Measurements of TPCE were performed using a standard Hanbury Brown-Twiss setup. The photons were counted by two identical detection setups, each consisting of an avalanche photodiode (APD) (SPD-050-CTE; Micro Photon Devices) and a time-correlated single-photon counting (TCSPC) board (SPC-130EM; Becker & Hickl GmbH). The TCSPC boards were operated in the time-tag mode, which enabled us to analyze both the $g^{(2)}$ and the PL-decay curves using the same data. We studied CdSe/ZnS NCs (Qdot655; Life Technologies Corporation) under two different excitation conditions. One arrangement permitted studying the neutral condition under weak excitation (4.2×10^{12} photons/cm^2). The other arrangement permitted the ionized condition under strong excitation (2.4×10^{13} photons/cm^2). In the Appendix, we show a TEM image and the linear absorption spectrum of our sample. We achieved the optical excitation of the NCs by using pulsed light, with a pulse width of about 50 ps, obtained from a supercontinuum light source (SC400-4-PP; Fianium) using a repetition rate of 5 MHz. The excitation wavelength was set to 430 nm using a tunable filter (SuperChrome; Fianium). The total detection efficiency was estimated to be 5 ~ 10%. The detection wavelength of the system was limited to the range between 700 and 625 nm using suitable sets of long-pass and short-pass filters. The details of the experimental setup appeared in a previous paper [24]. All measurements were performed at room temperature.

Converting the $g^{(2)}$ data and the PL decay curves to TPCE QY involves two equations,

$$\langle N \rangle = -ln\left[1 - 2\frac{g_S}{g_C} \cdot \frac{I_{XX}}{I_X}\left(1 + \frac{I_{XX}}{I_X}\right)^{-2}\right], \quad (1)$$

and

$$\frac{\eta_{XX}}{\eta_X} = \frac{I_{XX}}{I_X} \cdot \frac{P_X}{P_{XX}}, \quad (2)$$

where, respectively, g_S and g_C are the side and center peaks of the $g^{(2)}$ curve, I_{XX} and I_X are the PL intensity of the biexciton and exciton emissions, P_{XX} and P_X are the probabilities to populate the biexciton and exciton states in the NCs, and η_{XX} and η_X are the PL QY of the biexciton and exciton emissions. The value of η_{XX} is usually smaller than η_X due to an additional nonradiative recombination caused by Auger processes, in which the transition energy of an electron–hole pair is transferred to the additional charges [13-21]. Equation (2) defines the TPCE QY. By considering a Poisson distribution, $P(\langle N\rangle, m) = \langle N\rangle^m \exp(-\langle N\rangle)/m!$, for the incident light pulse, the term P_{XX} and P_X can be calculated as follows: $P_{XX} = \sum_{m=2}^{\infty} P(\langle N\rangle, m) = 1 - \exp(-\langle N\rangle) - \langle N\rangle \exp(-\langle N\rangle)$ and $P_X = \sum_{m=1}^{\infty} P(\langle N\rangle, m) = 1 - \exp(-\langle N\rangle)$. The effect of PL saturation is included in these terms P_{XX} and P_X. The value of $\langle N\rangle$ is connected to the absorption cross section σ of the NCs by means of the relation $\sigma = \langle N\rangle/j$, where j is the excitation photon flux.

We consider that Eqs. (1) and (2) are valid for both the neutral and the ionized systems. For the ionized system, the descriptions of XX and X in Eqs. (1) and (2) must be changed to XX^- (charged biexcitons) and X^- (charged excitons), respectively. We also assume that the ionization does not change σ of a single NC. This assumption provides a good approximation because the present experiments were performed with excitation photon energies much larger than the PL photon energies. In the Appendix section, we present a detailed description of the derivations of Eqs. (1) and (2). In addition, the Appendix also explains the differences between Eqs. (1) and (2) and those reported in our previous paper [24]. It is notable that all contribution of XX and X emission during TPCE are included in Eqs. (1) and (2). This means that, by measuring simultaneously both the $g^{(2)}$ and PL-decay curves, the QY of the TPCE can be determined even under strong-excitation conditions.

III. RESULTS AND DISCUSSION

First, we show representative data for evaluating the TPCE QY in a single NC. Fig. 2(a) and 2(b) show the time dependence of PL intensity and lifetime, respectively. The data were plotted with a binning (bin) time of 50 ms. The excitation density was 4.2×10^{12} photons/cm^2 and the total measurement time was 200 s. The lifetime was determined by applying a single-exponential fit to the data in each bin interval [6,24]. The decay curve obtained for the bin at 17.0 s is plotted in Fig. 2(c). High PL intensities with count rates above 70 kHz were observed frequently. The relationship between PL lifetime and intensity, which is known as fluorescence lifetime-intensity distribution (FLID), is presented in Fig. 2(c), where y-axis units are cts/bin. The main contribution with large PL intensities (3500–4000 cts/bin) and long lifetimes (28–50 ns) is attributed to the signal for the neutral

conditions, which are dominated by PL of neutral excitons.

The additional contribution with small intensities (1900–2200 cts/bin) and the short lifetimes (9–14 ns) is attributed to the signal for ionized conditions, which are dominated by the PL of charged excitons [36–40]. Because the bin time of 50 ms is not short enough to resolve these two contributions completely, the signal dominated by both neutral and charged excitons during the bin time appears between the contributions of neutral and charged excitons [38,39]. Fig. 2(d) through 2(g) show the data measured under strong-excitation power of 2.4×10^{13} photons/cm^2. The decay curves obtained for the bin at 13.0 s is plotted in Fig. 2(g). These data were plotted with a bin time of 20 ms. Compared to the weak-excitation condition, the PL fluctuation becomes frequent. The signal of the charged excitons, indicated by the yellow rectangle in Fig. 2(h), was obtained with a count rate of around 100 kHz.

Because our measurements were conducted using the time-tagged mode, the events of photon detection can be extracted from any specific region in the FLID [24]. In Figs. 3(a) and 3(b), we plotted the results of the analysis of the PL decay curve and the $g^{(2)}$ curves obtained from the data located in the yellow rectangle in Fig. 2(h). The dotted line in Fig. 3(a) is a single exponential function fitted to the slow decay component with a time range of 10 ns to 50 ns. The curve plotted in Fig. 3(c) was obtained by subtracting the fitting result from the experimental data. Then, by applying a further single exponential fitting to this subtracted data (dotted line), the lifetime of the fast decay component was estimated to be 1.3 ns.

These fast and slow decay components are attributed to the emission of charged biexcitons and charged excitons, respectively. We verified these assignments and obtained accurate evaluations of I_{XX^-}/I_{X^-} and g_C/g_S by performing two sophisticated analyses. In the first, called time-gated $g^{(2)}$ analysis, the $g^{(2)}$ curve was analyzed by applying a time gate to the PL decay curve [29–31]. Considering that the contribution of the fast decay component becomes negligible at 5 ns, we chose 5 ns for the threshold of the time gate, i.e., only data after 5 ns was considered. Fig. 3(d) plots the result of the time-gated $g^{(2)}$ analysis. A clear disappearance of the center peak in the $g^{(2)}$ curve is observed. This result means that the center peak in Fig. 3(b) reflects the TPCE contribution and thus the g_C/g_S ratio in Eq. (1) can be evaluated from the data. The other analysis method, which we call first-photon decay analysis, examines the PL-decay curve of the first photons in the center peak of the $g^{(2)}$ data [18,19,23]. This is achieved by the time-tag mode measurements, which enable us to extract the data of the first photon emission of TPCE from the two-photon detection events counted in the $g^{(2)}$ center peak. By applying this analysis to the $g^{(2)}$ data in Fig. 3(b), we obtain the PL decay curve shown in Fig. 3(e). The dashed curve is a single exponential function with a lifetime of 1.3 ns, which is the

same curve as shown in Fig. 3(c). The agreement between the theoretical curve and the experimental data confirms that the data in Fig. 3(c) represents the decay of the charged biexciton emissions. From the data in Figs. 3(a) and 3(c), I_{XX^-}/I_{X^-} is determined to be 0.14. From the data in Fig. 3(b), g_C/g_S is evaluated to be 0.41. By inserting these values into Eq. (1), the value of $\langle N \rangle$ is determined to be 0.75.

When the same analysis was performed for the signal dominated by the neutral exciton PL, which appeared in the region with intensities in the range 3400 cts/bin to 4000 cts/bin and lifetimes between 29 ns to 33 ns, as depicted in Fig. 2(c), we obtained $\langle N \rangle = 0.14$ (analysis is presented in the Appendix section). The ratio between the values of $\langle N \rangle$, 5.4, is almost consistent with the ratio, 5.7, of the value of the excitation power. This agreement means that $\langle N \rangle = 0.75$ is correct, even though this data was for relatively strong-excitation. By inserting $\langle N \rangle = 0.75$ and $I_{XX^-}/I_{X^-} = 0.14$ into Eq. (2), the value of η_{XX^-}/η_{X^-} was determined to be 0.43. When a similar calculation was performed for the signal of exciton PL, we obtained $\eta_{XX}/\eta_X = 0.23$. With the use of Eqs. (1) and (2), both η_{XX}/η_X and η_{XX^-}/η_{X^-} for single NCs were successfully evaluated.

Next, we show the results of the TPCE QY measured for 25 particles. Each NC was studied under excitation with 2.4×10^{13} photons/cm^2 and 4.2×10^{12} photons/cm^2, from which the values of η_{XX^-}/η_{X^-} and η_{XX}/η_X were determined, respectively. Fig. 4(a) plots the results of η_{XX^-}/η_{X^-} (blue diamonds) and the results of g_C/g_S (open diamonds) as functions of $\langle N \rangle$. The values of $\langle N \rangle$ are distributed in a wide range from 0.6 to 1.5, probably because of the inhomogeneity of σ of the single NCs [24]. The overall large values of $\langle N \rangle$ are consistent with the fact that the data were recorded under strong-excitation condition. The values of η_{XX^-}/η_{X^-} are distributed between 0.4 and 1.0, and the values of g_C/g_S are distributed between 0.4 and 0.6. Fig. 4(b) plots the results of η_{XX}/η_X (red diamonds) and g_C/g_S (open diamonds) as functions of $\langle N \rangle$ obtained under the weak-excitation condition. Both η_{XX}/η_X and g_C/g_S are distributed in the range from 0.1 to 0.3. The values of $\langle N \rangle$ are within 0.1 to 0.4. As expected, for the neutral condition, where $\langle N \rangle$ is much smaller than unity, η_{XX}/η_X is almost the same as g_C/g_S [13,14]. In contrast, for the ionized condition, where $\langle N \rangle$ is relatively large, η_{XX^-}/η_{X^-} differs from g_C/g_S.

To understand the mechanism behind the results, we calculate the g_C/g_S ratio as a function of $\langle N \rangle$ for various values of η_{XX}/η_X. For the calculation, we used Eqs. (1) and Eqs. (2) to derive;

$$\frac{g_C}{g_S} = \frac{2P_{XX}}{P_X{}^2} \cdot \frac{\eta_{XX}}{\eta_X} \cdot \left(1 + \frac{P_{XX} \cdot \eta_{XX}}{P_X \cdot \eta_X}\right)^{-2}. \quad (3)$$

Fig. 5 shows the calculated results for η_{XX}/η_X ranging from 0.01 to 0.7. It is clear that, for $\langle N \rangle \ll 1$, the values of g_C/g_S agree with η_{XX}/η_X. When the value of $\langle N \rangle$ approaches unity, the value of g_C/g_S

gradually deviates from η_{XX}/η_X. Interestingly, the direction of the change can be either positive or negative. For the case of η_{XX}/η_X below 0.3, the discrepancy is positive, which means that the actual value of η_{XX}/η_X is smaller than g_C/g_S. In contrast, for the case of η_{XX}/η_X above 0.5, the discrepancy becomes negative. This negative discrepancy originates from the third term of the right side of Eq. (3), which becomes smaller than unity for large $\langle N\rangle$. Because of this effect, the results of η_{XX^-}/η_{X^-} in Fig. 4(a) showed negative discrepancies from g_C/g_S. These calculation results mean that, for the determination of the TPCE QY under strong-excitation condition ($\langle N\rangle > 0.5$), the current method can be more precise compared to the conventional method [13] based on $g^{(2)}$ measurement only. By examining the excitation power dependence of $\langle N\rangle$, we confirmed that the current method is valid even for $\langle N\rangle > 1$ (The results are provided in the Appendix). In the Appendix, we also discuss the contribution of triexcitons.

Let us further discuss the relationship between the TPCE QY and PL lifetimes. During the analysis of the TPCE QY for ionized and neutral conditions using Eqs. (1) and (2), the PL lifetimes of charged excitons (τ_{X^-}), charged biexcitons (τ_{XX^-}), excitons (τ_X), and biexcitons (τ_{XX}) were also evaluated. Given the values of the PL lifetimes and the TPCE QY, one can compare the radiative recombination rates of the first and second photon emissions [19]. In Figs. 6(a) and 6(b), the values of η_{XX^-}/η_{X^-} and η_{XX}/η_X are plotted as functions of τ_{XX^-}/τ_{X^-} and τ_{XX}/τ_X, respectively. These plots use the same sets of data as shown in Figs. 4(a) and 4(b). The black dashed lines are linear functions fitted to the experimental data. The slope of the line for the ionized condition was 3.5, and the slope for the neutral condition was 4.2. The ratio between the radiative recombination rates of the first and second photon emissions can be expressed by; $k_{R,XX^-}/k_{R,X^-} = (\eta_{XX^-}/\eta_{X^-})\cdot(\tau_{X^-}/\tau_{XX^-})$ and $k_{R,XX}/k_{R,X} = (\eta_{XX}/\eta_X)\cdot(\tau_X/\tau_{XX})$, where k_{R,X^-}, k_{R,XX^-}, $k_{R,X}$, and $k_{R,XX}$ are the radiative recombination rates of the X^-, XX^-, X, and XX states, respectively. Thus, using the slope of dotted lines in Figs. 6(a) and 6(b), we obtained $k_{R,XX^-}/k_{R,X^-} = 3.5$ and $k_{R,XX}/k_{R,X} = 4.2$, on average. These values are consistent with the statistical scaling law explained below.

According to the statistical scaling law available at room temperature [18–22], the increase in the radiative recombination rate is proportional to the numbers of electrons and holes. In the ionized condition, the scaling law predicts $k_{R,XX^-}/k_{R,X^-} = 3$, because the radiative recombination rates of XX^- states and X^- states are $6k_{R,X}$ and $2k_{R,X}$, respectively. In the neutral condition, the scaling law predicts $k_{R,XX}/k_{R,X} = 4$, because the radiative recombination pathway of the XX states is four times larger than the radiative recombination pathway of the X states. Our experimental results, showing $k_{R,XX^-}/k_{R,X^-} = 3.5$ and $k_{R,XX}/k_{R,X} = 4.2$, are almost consistent with these predictions of 3 and 4. This

agreement means that, in CdSe/ZnS NCs, the ratio between $k_{R,XX}$ and $k_{R,X}$ (k_{R,XX^-} and k_{R,X^-}, if the NC is ionized) is almost proportional to the product of the numbers of electrons and holes, as the scaling law predicts.

As we have shown in Figs. 4(a) and 4(b), the values of η_{XX^-}/η_{X^-} ranged from 0.4 to 0.9, and the values of η_{XX}/η_X ranged from 0.12 to 0.32. On average, η_{XX^-}/η_{X^-} was two times larger than η_{XX}/η_X. This difference can be explained by Auger processes due to their inherent nonradiative recombination [14–21]. As a result of the Auger process, η_{X^-} usually becomes smaller than η_X [36–40]. The data presented in Fig. 2(c) agrees with this Auger model because the PL intensity of the charged excitons is smaller than that of the neutral excitons. When the ratio between η_X and η_{X^-} is estimated from the PL intensities of the X and X^- emissions in Fig. 2(c), it was ~0.5. Similar values were also observed for other NCs. These observations mean that $1/\eta_{X^-}$ is two times larger than $1/\eta_X$. This fact, in conjunction with the fact that η_{XX^-}/η_{X^-} is two times larger than η_{XX}/η_X, indicates that η_{XX^-} is almost the same as η_{XX}. This result is interesting, because the QY of multi excitons usually becomes smaller when the number of charges increases. We believe that this result should be explained by the difference in Auger recombination rates of electrons and holes in CdSe/ZnS NCs [18,19,22]. If the Auger rate is determined by one of the charges, the ratio between the radiative and Auger rates can be the same for both biexcitons and charged biexcitons. In the present case, the Auger rate of holes should be larger than that of electrons [18,19,22]. Thus, η_{XX^-} could be almost the same as η_{XX}.

We finally note the importance of the technique we developed for the present experiment. A number of researchers have reported the measurement of the TPCE QY in various systems using a standard $g^{(2)}$ setup [13–24,27–35]. These experiments were performed under weak-excitation conditions, because the conversion from the $g^{(2)}$ curve to the QY of the TPCE could be performed only under $\langle N \rangle \ll 1$ [13,14]. We also used this weak-excitation approximation in our previous work, which introduced the determination method of the absorption cross section based on the measurements of the $g^{(2)}$ and PL decay curves [24]. In contrast, the present technique based on Eqs. (1) and (2) is available even for $\langle N \rangle \sim 1$. This is an advantage for the study of the TPCE under ionized conditions, since the appearance of ionized states can be increased under strong excitation conditions [40]. In our experiment, some of the particles did not show clear emission of ionized states under weak excitation conditions ($\langle N \rangle < 0.2$). For such case, it was difficult to determine the accurate values of η_{XX^-}/η_{X^-} and τ_{XX^-}. Our technique should be also important for other kinds of NCs, such as NCs emitting photons in the infrared region with low detection efficiency [16], NCs coupled with metal [27–32], and NCs composed of unique materials [33–35]. In these contexts, the excitation power needs to be high for

obtaining a sufficient signal. Furthermore, direct determination of $\langle N \rangle$ based on Eq. (1) is a powerful technique because only one simultaneous measurement of $g^{(2)}$ and PL-decay curves is needed, regardless of the excitation power. With this technique, it is not necessary to perform measurements of excitation-power dependent PL intensities, a conventional method for determining $\langle N \rangle$ from the data of PL saturation [14]. This is advantageous, because for fragile NCs, charging and degradation make observations of PL saturation difficult. We believe that the developed technique should be very useful for determining the TPCE QY in various NCs.

IV. CONCLUSION

In summary, we investigated PL lifetime and QY of TPCE on single CdSe/ZnS NCs using simultaneous measurements of both $g^{(2)}$ and PL decay curves. For the determination of the QY of TPCE under the strong-excitation condition, we developed an analysis technique considering the nonlinear effect of PL saturation and the increase of two-photon emission probability. With this technique, we successfully evaluated the TPCE QY in single CdSe/ZnS NCs, for both neutral and ionized conditions. We showed that the radiative recombination rates during TPCE are almost proportional to the product of the number of electrons and holes, even when the NCs are ionized. The developed technique permits the convenient evaluation of the TPCE QY and the radiative-recombination-rate ratio between the exciton and the biexciton emissions in various NCs.

ACKNOWLEDGMENTS

Part of the research reported in this paper was supported by JST-CREST (Grant No. JPMJCR16N3) and JSPS KAKENHI (Grant No. 16K17483).

APPENDIX A : SIZE AND SHAPE OF THE NCS

Figure A1 shows (a) a TEM image and (b) the linear absorption spectrum of the sample studied in our experiment (Qdot655). The shape of the sample is bullet-like. The orientation of the NCs should be random since we spin coat them on a cover glass. The values of absorption cross-section of this sample probably depend on the orientation of the single NCs. The inhomogeneity in size of the NCs also influences the absorption cross-section. The first absorption peak appeared at ~1.9 eV. Based on the relationship between core size and the first absorption peak energy reported by earlier works [42,43], we estimated the effective core diameter of our sample to be 8.2 nm.

APPENDIX B : DERIVATION OF EQUATIONS (1) AND (2).

When the PL lifetime is much shorter than the inverse of the repetition rate of the incident laser pulse, the $g^{(2)}$ curve can be separated into side and center peaks [24]. By taking into account the contributions of exciton and biexciton PL, the count rates of the side and center peaks, g_S and g_C, respectively, of the $g^{(2)}$ curves can be expressed by;

$$g_S = F \cdot (P_{XX} \cdot \eta_{XX} + P_X \cdot \eta_X)^2 \cdot \xi_A \cdot \xi_B, \tag{A1}$$

and

$$g_C = 2F \cdot P_{XX} \cdot \eta_{XX} \cdot \eta_X \cdot \xi_A \cdot \xi_B, \tag{A2}$$

where F is the repetition rate of the incident laser pulse. Here, for NCs, P_{XX} and P_X are the probabilities for populating the biexcitons and excitons, respectively; η_{XX} and η_X are the QY of biexciton and exciton emissions, respectively; ξ_A and ξ_B are the detection efficiencies of one of the optical path A and B, respectively, of the Hanbury Brown-Twiss setup. The contributions of PL from multi-excitons of higher order than biexcitons, i.e. triexcitons, were ignored. Using the same parameters, the PL intensities of excitons I_X and biexcitons I_{XX} can be written as

$$I_X = F \cdot P_X \cdot \eta_X \cdot (\xi_A + \xi_B), \tag{A3}$$

and

$$I_{XX} = F \cdot P_{XX} \cdot \eta_{XX} \cdot (\xi_A + \xi_B). \tag{A4}$$

From Eqs. (A1) thorough (A4), the following equation can be derived;

$$P_X = 2 \cdot \frac{g_S}{g_C} \cdot \frac{I_{XX} \cdot I_X}{(I_{XX} + I_X)^2}. \tag{A5}$$

By considering a Poisson distribution for the photon population in the incident pulse, the left-hand term in Eq. (A5) can be written as $P_X = \sum_{m=1}^{\infty} P(\langle N \rangle, m) = 1 - \exp(-\langle N \rangle)$. Thus, we obtain

$$\langle N \rangle = -ln\left[1 - 2\frac{g_S}{g_C} \cdot \frac{I_{XX} \cdot I_X}{(I_{XX} + I_X)^2}\right]. \tag{A6}$$

This equation appears in the main body of the paper as Eq. (1). In addition, from Eqs. (A3) and (A4), the following equation can be derived;

$$\frac{I_X}{I_{XX}} = \frac{P_X \cdot \eta_X}{P_{XX} \cdot \eta_{XX}}. \tag{A7}$$

This equation can be converted to Eq. (2) as presented in the manuscript.

APPENDIX C : CALCULATION OF $\langle N \rangle$ BASED ON THE EQUATIONS

In the previous paper [1], the following equation was used to determine the absorption cross section of single NCs;

$$\sigma \cdot j = \langle N \rangle = -ln\left[1 - 2\frac{g_S}{g_C} \cdot \frac{A_{XX} + B_{XX}}{A_X + B_X}\right], \tag{A8}$$

where $A_{XX} + B_{XX}$ and $A_X + B_X$ correspond to I_{XX} and I_X, respectively. This equation assumes that the

contribution of the biexciton PL to the side peak in the $g^{(2)}$ curve is negligible. With this approximation, Eq. (A1) can be expressed as;

$$g_{\mathrm{S}} = F \cdot {P_X}^2 \cdot {\eta_X}^2 \cdot \xi_{\mathrm{A}} \cdot \xi_{\mathrm{B}}. \tag{A9}$$

In contrast, Eq. (1) includes the contribution of biexcitons to the side peak in the $g^{(2)}$ curve. Because of this improvement, Eq. (1) becomes available under strong-excitation conditions. To see the difference between Eqs. (1) and (A8), we would like to calculate $\langle N \rangle$ using these two equations and then compare the results.

In Fig. A2(a), we plot $\langle N \rangle' / \langle N \rangle_0$ as a function of $\langle N \rangle_0$ for various values of η_{XX}/η_X, where $\langle N \rangle'$ is the results calculated using Eq. (A8), and $\langle N \rangle_0$ is the fixed value of $\langle N \rangle$. For the calculation of $\langle N \rangle'$, Eqs. (A2), (A3), (A4), and (A9) were used. For larger $\langle N \rangle_0$ and for larger η_{XX}/η_X, the discrepancy of $\langle N \rangle'$ from $\langle N \rangle_0$ becomes large. When $\eta_{XX}/\eta_X = 0.5$, the discrepancy of $\langle N \rangle'$ from $\langle N \rangle_0$ becomes 10 % at relatively small $\langle N \rangle_0$ of approximately 0.2. When $\eta_{XX}/\eta_X = 0.05$, on the other hand, the discrepancy of $\langle N \rangle'$ from $\langle N \rangle_0$ becomes 10 % at relatively large $\langle N \rangle_0$ of approximately 1.5.

In Fig. A2(b), we plot $\langle N \rangle$ calculated from Eq. (1) as a function of j for various values of σ. For the calculation of $\langle N \rangle$, Eqs. (A1), (A2), (A3), and (A4) were used. $\langle N \rangle$ clearly increases linearly with j and σ. The linear relations between $\langle N \rangle$ and j resulted from the fact that Eq. (1) did not include any approximation of the biexciton contribution. The value of η_{XX}/η_X does not affect the calculated results. These calculated results mean that Eq. (1) is available for determining $\langle N \rangle$ regardless of η_{XX}/η_X, σ, and $\langle N \rangle_0$.

APPENDIX D : THE SETS OF DATA FOR NEUTRAL CONDITION

We extracted the data, depicted in Fig. 1(e), for neutral conditions from the region with intensities between 3400 cts/bin and 4000 cts/bin and lifetimes between 29 ns and 33 ns. The results of the PL decay curve and the $g^{(2)}$ curve are plotted in Figs. A3(a) and A3(b), respectively. The black dashed line in Fig. A3(a) presents the single-exponential fit to the data, where the fast-decay contribution was excluded from the fitting. By subtracting the fitting result from the experimental data, we obtained the contribution of the fast decay, as plotted in Fig. A3(c). By applying a single-exponential fitting to this subtracted data, the lifetime of the fast decay component was estimated to be 1.7 ns. The fast and slow decay components are attributed to the emission of biexcitons and neutral excitons, respectively. Figure A3(d) plots the result of the time-gated $g^{(2)}$ analysis, where we chose 5 ns for the threshold of the time gate. The disappearance of the center peak of the $g^{(2)}$ curve means that $g_{\mathrm{C}}/g_{\mathrm{S}}$ can be evaluated from the data in Fig. A3(b). By applying the first photon decay analysis on the $g^{(2)}$ data in Fig. A3(b), we obtain the decay curve shown in Fig. A3(e). The black dashed curve, which is the same curve as shown in Fig. A3(c), is a single exponential function with a lifetime of 1.7 ns. The agreement

between the theoretical curve and the experimental data confirms that the data in Fig. A3(c) presents the decay of the biexcitons. From the data in Figs. A3(a) and A3(c), I_{XX}/I_X is determined to be 0.016. From the data in Fig. A3(b), g_C/g_S is evaluated to be 0.24. By inserting these values into Eq. (1), $\langle N \rangle$ is determined to be 0.14.

APPENDIX E : EXCITATION POWER DEPENDENCE

Figure A4 shows additional experimental results of $\langle N \rangle$ measured for neutral conditions at different value of the incident photon flux. The red and black dots were obtained using Eqs. (1) and (A8), respectively. The red line is a linear function fitted to the red dots. The red dots clearly show linear dependence on j; in contrast, the black dots increase nonlinearly for $\langle N \rangle > 0.5$. At large values of j ($= 3.6 \times 10^{13}$ cm^{-2}), $\langle N \rangle$ could not be determined, because the antilogarithm became a negative value. As long as Eq. (1) was used, the value of $\langle N \rangle$ could be determined even under strong-excitation conditions.

APPENDIX F : CONSIDERATION OF TRIEXCITON EMISSION

A strong excitation condition leads to formation of higher order multiexcitons with significant probabilities. For $\langle N \rangle$ = 0.75, the probability of creating a triexciton is equal to 25 % of that for biexciton creation. To estimate the count rate of the triexciton emission, the QY of the triexciton, η_{XXX}, has to be estimated. According to the statistical scaling law, the radiative QY ratio of triexciton to biexciton, $\frac{\eta_{XXX}}{\eta_{XX}}$, is $\frac{2}{3}$ since the number of radiative recombination pathways of triexciton and biexciton are 4 and 9, respectively, and the number of Auger recombination pathways of triexciton and biexciton are 4 and 18, respectively. The count rate ratio of the triexciton and biexciton emission would then be $\frac{1}{6}$ for $\langle N \rangle$ = 0.75. This issue becomes a crucial problem when evaluating $\langle N \rangle$ and the TPCE QY in case that the triexciton emission wavelength is equivalent to the exciton emission wavelength. Fortunately, the triexciton emission is blue-shifted to the exciton emission by tens of meV in standard CdSe NCs [44,45]. Therefore, the triexciton emission can be cut by using an appropriate long-pass filter. In our experiment, we used a long-pass filter with cutoff wavelength at 625 nm, which could be suuficiently high to suppress triexciton detection.

REFERENCES

[1] D. V. Talapin, J. S. Lee, M. V. Kovalenko, and E. V. Shevchenko, Chem. Rev. **110**, 389 (2010).

[2] Y. Shirasaki, G. J. Supran, M. G. Bawendi, and V. Bulović, Nat. Photon. **7**, 13 (2013).

[3] K. D. Wegner and N. Hildebrandt, Chem. Soc. Rev. **44**, 4792 (2015).

[4] X. Brokmann, L. Coolen, M. Dahan, and J. P. Hermier, Phys. Rev. Lett. **93**, 107403 (2004).

[5] B. Fisher and H. Eisler, J. Phys.Chem. B **108**, 143 (2004).

[6] T. Ihara and Y. Kanemitsu, Phys. Rev. B **92**, 155311 (2015).

[7] S. Berciaud, L. Cognet, and B. Lounis, Nano Lett. **5**, 2160 (2005).

[8] P. Kukura, M. Celebrano, A. Renn, and V. Sandoghdar, J. Phys. Chem. Lett. **1**, 3323 (2010).

[9] J. Giblin, F. Vietmeyer, M. P. McDonald, and M. Kuno, Nano Lett. **11**, 3307 (2011).

[10] H. Baida, A. Crut, P. Maioli, T. B. Nguyen, D. H. Nguyen, N. Del Fatti, and F. Vallée, Adv. Nat. Sci. Nanosci. Nanotechnol. **2**, 035011 (2011).

[11] J. Cui, A. P. Beyler, T. S. Bischof, M. W. B. Wilson, and M. G. Bawendi, Chem. Soc. Rev. **43**, 1287 (2014).

[12] M. J. Ferné, P. Tamarat, and B. Lounis, Chem. Soc. Rev. **43**, 1311 (2014).

[13] G. Nair, J. Zhao, and M. Bawendi, Nano Lett. **11**, 1136 (2011).

[14] Y. S. Park, A. V. Malko, J. Vela, Y. Chen, Y. Ghosh, F. García-Santamaría, J. A. Hollingsworth, V. I. Klimov, and H. Htoon, Phys. Rev. Lett. **106**, 187401 (2011).

[15] J. Zhao, O. Chen, D. B. Strasfeld, and M. G. Bawendi, Nano Lett. **12**, 4477 (2012).

[16] T. S. Bischof, R. E. Correa, D. Rosenberg, E. A. Dauler, and M. G. Bawendi, Nano Lett. **14**, 6787 (2014).

[17] B. D. Mangum, Y. Ghosh, J. a Hollingsworth, and H. Htoon, Opt. Express **21**, 7419 (2013).

[18] Y. S. Park, W. K. Bae, J. M. Pietryga, and V. I. Klimov, ACS Nano **8**, 7288 (2014).

[19] Y. S. Park, W. K. Bae, L. A. Padilha, J. M. Pietryga, and V. I. Klimov, Nano Lett. **14**, 396 (2014).

[20] M. Nasilowski, P. Spinicelli, G. Patriarche, and B. Dubertret, Nano Lett. **15**, 3953 (2015).

[21] S. Sampat, N. S. Karan, T. Guo, H. Htoon, J. A. Hollingsworth, and A. V. Malko, ACS Photonics **2**, 1505 (2015).

[22] M. Manceau, S. Vezzoli, Q. Glorieux, F. Pisanello, E. Giacobino, L. Carbone, M. De Vittorio, and A. Bramati, Phys. Rev. B **90**, 035311 (2014).

[23] D. Canneson, L. Biadala, S. Buil, X. Quelin, C. Javaux, B. Dubertret, and J. P. Hermier, Phys. Rev. B **89**, 035303 (2014).

[24] T. Ihara, Phys. Rev. B **93**, 235442 (2016).

[25] Y. Yang, Y. Zheng, W. Cao, A. Titov, J. Hyvonen, J. R. Manders, J. Xue, P. H. Holloway, and L. Qian, Nat. Photon. **9**, 259 (2015).

[26] J. M. Pietryga, Y.-S. Park, J. Lim, A. F. Fidler, W. K. Bae, S. Brovelli, and V. I. Klimov, Chem.

Rev. **116**, 10513 (2016).

[27] Y. S. Park, Y. Ghosh, Y. Chen, A. Piryatinski, P. Xu, N. H. Mack, H. L. Wang, V. I. Klimov, J. A. Hollingsworth, and H. Htoon, Phys. Rev. Lett. **110**, 117401 (2013).

[28] S. J. Leblanc, M. R. McClanahan, M. Jones, and P. J. Moyer, Nano Lett. **13**, 1662 (2013).

[29] H. W. Cheng, C. T. Yuan, J. S. Wang, T. N. Lin, J. L. Shen, Y. J. Hung, J. Tang, and F. G. Tseng, J. Phys. Chem. C **118**, 18126 (2014).

[30] F. Wang, N. S. Karan, H. M. Nguyen, B. D. Mangum, Y. Ghosh, C. J. Sheehan, J. A. Hollingsworth, and H. Htoon, Small **11**, 5028 (2015).

[31] Y. Gao, O. Roslyak, E. Dervishi, N. S. Karan, Y. Ghosh, C. J. Sheehan, F. Wang, G. Gupta, A. Mohite, A. M. Dattelbaum, S. K. Doorn, J. A. Hollingsworth, A. Piryatinski, and H. Htoon, Adv. Opt. Mater. **3**, 39 (2015).

[32] S. Masuo, K. Kanetaka, R. Sato, and T. Teranishi, ACS Photonics **3**, 109 (2016).

[33] Y. S. Park, S. Guo, N. S. Makarov, and V. I. Klimov, ACS Nano **9**, 10386 (2015).

[34] F. Hu, H. Zhang, C. Sun, C. Yin, B. Lv, C. Zhang, W. W. Yu, X. Wang, Y. Zhang, and M. Xiao, ACS Nano **9**, 12410 (2015).

[35] G. Rainò, G. Nedelcu, L. Protesescu, M. I. Bodnarchuk, M. V. Kovalenko, R. F. Mahrt, and T. Stöferle, ACS Nano **10**, 2485 (2016).

[36] D. E. Gómez, J. Van Embden, P. Mulvaney, M. J. Fernée, and H. Rubinsztein-Dunlop, ACS Nano **3**, 2281 (2009).

[37] P. Spinicelli, S. Buil, X. Quélin, B. Mahler, B. Dubertret, and J. P. Hermier, Phys. Rev. Lett. **102**, 136801 (2009).

[38] C. Galland, Y. Ghosh, A. Steinbrück, J. a Hollingsworth, H. Htoon, and V. I. Klimov, Nat. Commun. **3**, 908 (2012).

[39] C. Galland, Y. Ghosh, A. Steinbrück, M. Sykora, J. a Hollingsworth, V. I. Klimov, and H. Htoon, Nature **479**, 203 (2011).

[40] N. Yoshikawa, H. Hirori, H. Watanabe, T. Aoki, T. Ihara, R. Kusuda, C. Wolpert, T. K. Fujiwara, A. Kusumi, Y. Kanemitsu, and K. Tanaka, Phys. Rev. B **88**, 155440 (2013).

[41] T. Ihara and Y. Kanemitsu, Phys. Rev. B **90**, 195302 (2014).

[42] T. J. Liptay, L. F. Marshall, P. S. Rao, R. J. Ram, and M. G. Bawendi, Phys. Rev. B **76**, 155314 (2007).

[43] M. Kuno, J. K. Lee, B. O. Dabbousi, F. V. Mikulec, and M. G. bawendi, J. Chem. Phys. **106**, 9869 (1997).

[44] C. Bonati, M. B. Mohamed, D. Tonti, G. Zgrablic, S. Haacke, F. van Mourik, and M. Chergui, Phys. Rev. B **71**, 205317 (2005).

[45] B. Fisher, J. M. Caruge, D. Zehnder, and M. G. Bawendi, Phys. Rev. Lett. **94**, 087403 (2005).

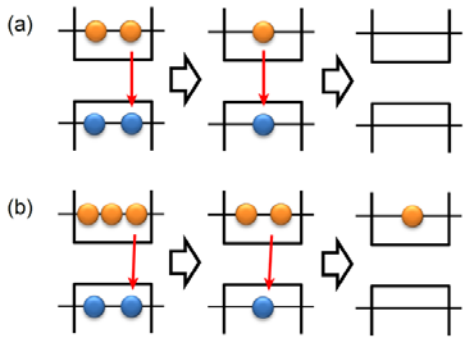

Figure 1. (Color online) Schematics of the two-photon cascade emission (TPCE) process for (a) neutral NCs and (b) ionized NCs.

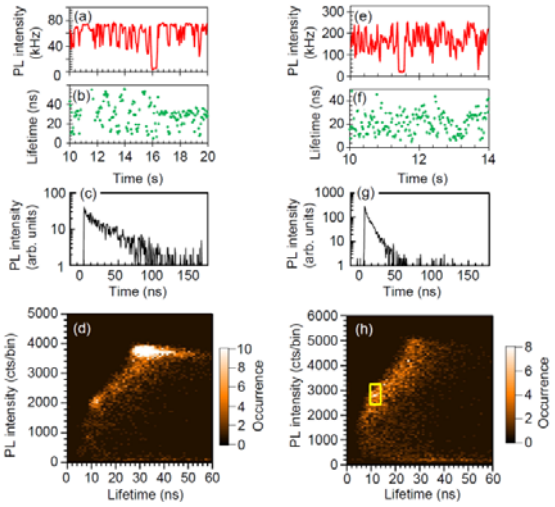

Figure 2. (Color online) PL dynamics of a single CdSe/ZnS NC measured for an excitation photon flux of (a–d) and (e–h). The PL intensities are plotted as function of time with a bin time of (a) 50 ms and (b) 20 ms. In (b) and (f), the corresponding lifetimes are plotted. The lifetimes were obtained by fitting the decay curve of each bin. The decay curve for the single bin time at 17 s in (a) and that at 13 s in (e) are shown in (c) and (g), respectively. In (d) and (h), the correlation between PL intensity and lifetime is plotted for all bins of the respective measurement. For this correlation plot, the data was recorded for 200 s. The x axis is given in units of ns, and corresponds to the lifetime obtaioned from the fitting process of the PL decay in each bin. The yellow rectangle in (h) represents the region with PL intensity between 2400 and 3200 cts/bin and lifetime between 10 and 14 ns.

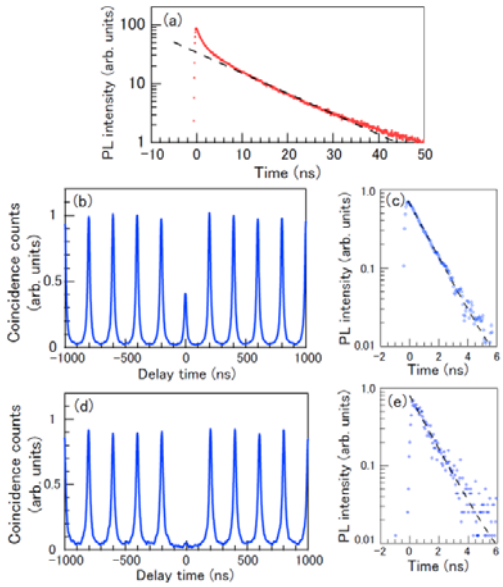

Figure 3. (Color online) Results of (a) PL decay curve (red dots) and (b) $g^{(2)}$ curve derived from the data within the yellow rectangle indicated in Fig. 2(c). The black dashed line in (a) is an exponential function fitted to the data. The fitting range was set from 10 to 50 ns. (c) The PL decay curve of the charged-biexciton emission (blue dots) obtained by subtracting the black dashed line from the experimental data in (a). The black dashed line in (c) is a single exponential function with a lifetime of 1.3 ns, which was obtained from fitting the data. (d) The result of the time-gated $g^{(2)}$ analysis. The threshold for the time gate was set to 5 ns. (e) The result of the first-photon decay analysis (blue dots). The black dashed line in (e) is a single exponential function with lifetime of 1.3 ns.

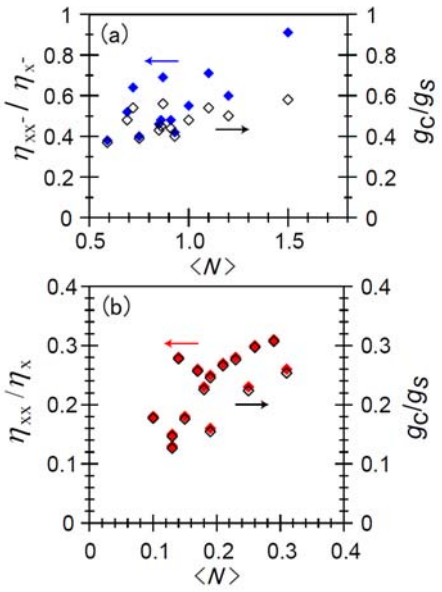

Figure 4. (Color online) Values of TPCE QY (solid diamonds) and (open diamonds) plotted as a function of measured for (a) ionized condition under strong-excitation and (b) neutral conditions under weak excitation. The values of were derived from and (or) using Eq. (1). The values of and were derived from and (or) using Eq. (2).

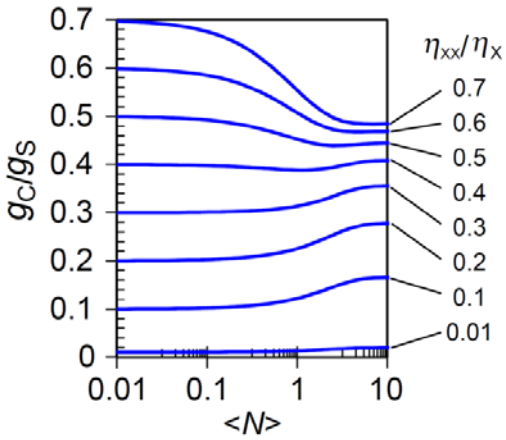

Figure 5. (Color online) Relation between and calculated for different values of . The calculation was performed using Eq. (3). When is large, differs from . In the case of , the value of is smaller than . In the case , the value of is larger than .

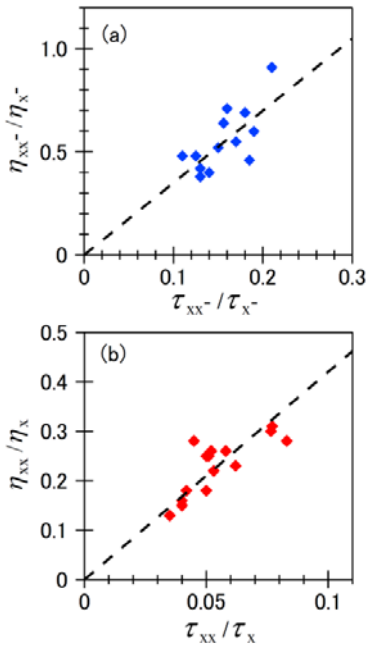

Figure 6. (Color online) (a) Results of plotted as a function of (blue diamonds). The black dashed line is a linear function fitted to the data with a slope of 3.5. (b) Results of plotted as a function of (red diamonds). The black dashed line is a linear function fitted to the data with a slope of 4.2.

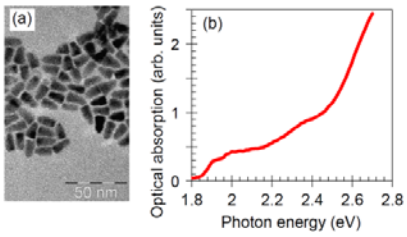

Figure A1. (Color online) (a) TEM image and (b) linear absorption spectrum of the sample studied in our experiments (Qdot655).

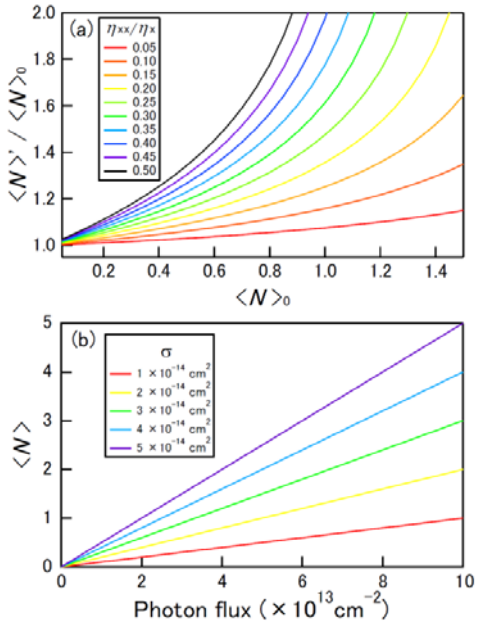

Figure A2. (Color online) (a) calculated as a function of for various ratios of , where is fixed to and is calculated using Eqs. (A2), (A3), (A4), and (A8). (b) calculated from Eq. (1) as a function of for various values of .

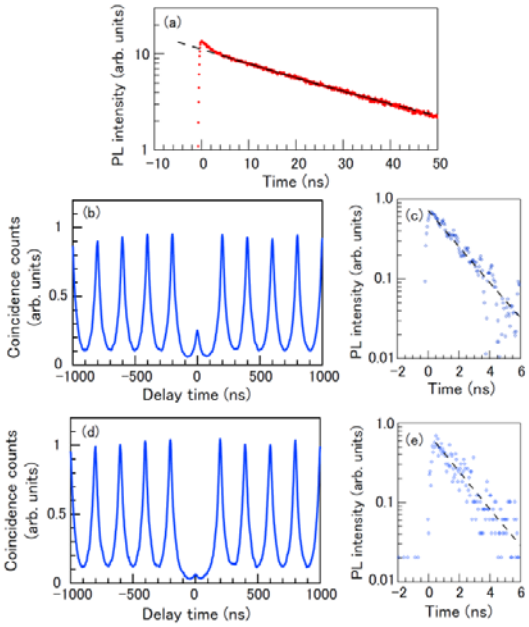

Figure A3 (Color online) Results of (a) PL decay curve (red dots) and (b) $g^{(2)}$ curve for neutral condition. These curves were derived from the data with intensities between 3400 and 4000 cts/bin and lifetimes between 29 and 33 ns. The black dashed line in (a) is an exponential function fitted to the data. The fitting range was set from 10 to 50 ns. (c) The PL decay curve of the biexciton emission (blue dots) obtained by subtracting the black dashed line from the experimental data in (a). The black dashed line in (c) is a single exponential function with a lifetime of 1.7 ns, which was obtained from fitting the data. (d) The result of the time-gated $g^{(2)}$ analysis. The threshold for the time gate was set to 5 ns. (e) The result of the first-photon decay analysis (blue dots). The black dashed line in (e) is a single exponential function with lifetime of 1.7 ns.

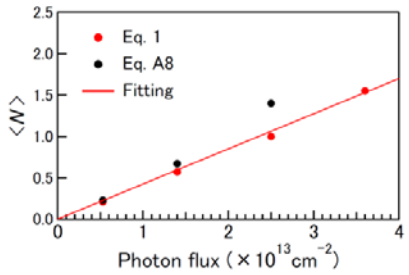

Figure A4. Experimental results of evaluated using Eq. (1) (Red dots) and Eq. (A8) (Black dots) for various photon fluxes. The red solid line is the linear function fitted to the red dots. At large values of ( ), could not be determined using Eq. (A8) because of a negative argument in the logarithm.